Article

Metal Coordination Induces Phase Segregation in Amphipolar Arborescent Copolymers with a Core−Shell−Corona Architecture

Jason Dockendorff, Ahmed Mourran,* Rustam A. Gumerov, Igor I. Potemkin,* Martin Möller, and Mario Gauthier*

Read Online

ACCESS | Metrics & More | Article Recommendations | Supporting Information

ABSTRACT: Arborescent copolymers with a core−shell−corona (CSC) architecture were synthesized and the topology of the molecules was challenged (constrained) through intramolecular interactions, resulting in phase separation breaking the symmetry of radial density. The inner poly(2-vinylpyridine) shell of these arborescent polystyrene-*g*-[poly(2-vinylpyridine)-*b*-polystyrene] molecules can self-assemble by binding metallic salts and acids in apolar and intermediate-polarity solvents. Upon loading with HAuCl₄, the characteristics of the polymer templates govern the "loading sites" of the metal within the molecules. Unique morphologies were observed for the metal-loaded G0−G4 arborescent copolymers investigated, namely, spherical, toroidal, raspberry-like, spherical nanocage, and a new worm-in-sphere morphology. The reason for the emergence of such morphologies is the interplay among intramolecular interactions of unlike polymer segments, solvent selectivity, the entropic elasticity of the arborescent substrate, and phase segregation induced by coordination with the charged metallic species. Meanwhile, the stability of the arborescent molecules against aggregation provides intramolecular phase segregation with imposed "confined" geometry and thus leads to nonconventional morphologies. Furthermore, the size of the arborescent molecules is much smaller than that of other known particles (droplets) serving as confined geometries. Computer simulations were used to model the mesostructure of the arborescent copolymers, to demonstrate the influence of solvent selectivity, together with HAuCl₄ loading, on the evolution of the morphology of the macromolecules.
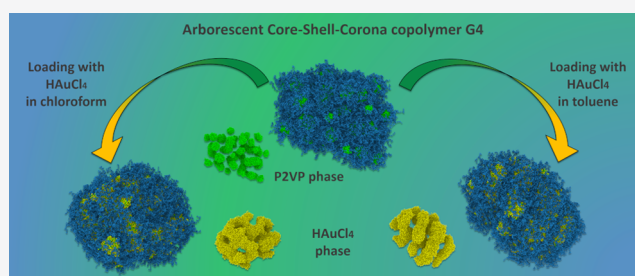
INTRODUCTION

Arborescent polymers, also known as dendrigraft polymers, are macromolecular objects with an open structure resulting from successive grafting reactions.[1−3] Similar to dendrimers and in contrast to hyperbranched polymers, the molecular structure of arborescent polymers is well-defined since their building blocks are relatively monodisperse linear chains, which are grafted onto polymeric substrates in a generation-based scheme, leading to a radial distribution of monomer density and a diffuse outer boundary. The increase in density of these materials is consistent with geometric growth approaching a dense sphere, as successive generations have higher branching functionalities (total number of grafts) and molecular weights. While the correlation between density and arborescent topology, i.e., how the polymer branches are linked to each other within the constraints of three-dimensional space, is a well-studied subject, very little is known on how intramolecular interactions induce density variations evolving into microphase separation. Different synthetic strategies have been developed for the production of arborescent molecules, allowing the preparation of multicomponent macromolecules based on regular polymers[4−8] and polyelectrolytes.[9,10] Since the number of grafts and their chemical composition can be varied in each

generation, highly branched copolymers can be obtained. The solution properties of arborescent copolymers, such as their ability to elude aggregation and form unimolecular micelles,[4,9,10] can give rise to a number of contemporary applications for these multicomponent molecules, like templates for the formation of metallic nanoparticles of predefined shape,[11,12] or microcapsules for efficient drug delivery.[8]

Despite the progress achieved so far, there are still questions to be addressed, such as the extent to which connectivity and topology of the macromolecular network reduces conformational freedom. In particular, arborescent (co-)polymers are less dense than their dendritic analogues, which offers a latent entropic elasticity enabling intramolecular phase segregation under topological constraints. This issue is addressed herein, by incorporating incompatible polymer segments buried in the
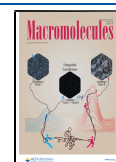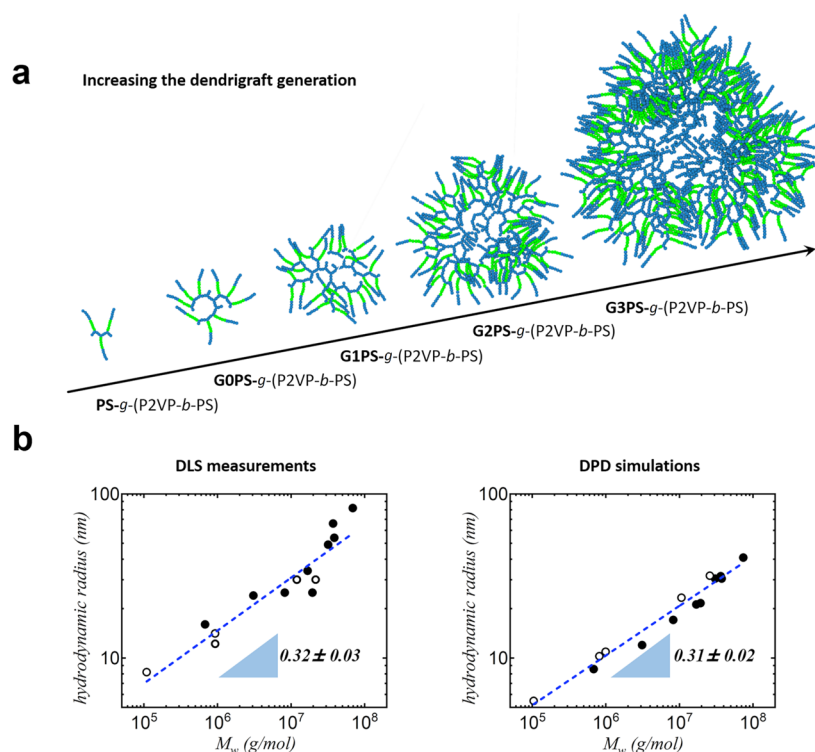
Figure 1. Arborescent CSC copolymers: (a) schematic model for arborescent macromolecules of generation number G_{x+1} = GxPS-g-(P2VPn-b-PSm); (b) scaling exponent for the hydrodynamic radius of arborescent polymers with molecular weight in toluene solutions obtained from dynamic light-scattering (DLS) measurements (left plot) and dissipative particle dynamics (DPD) simulations (right plot). The open symbols correspond to the PS arborescent substrates (Tables 1 and S4), and the full symbols correspond to the CSC copolymers (Tables 2 and S4).

arborescent polymer near the outer shell, which mediates interactions with their environment. Grafting chemically incompatible side chains at the diffuse boundary can modify the internal structure and induce intramolecular phase segregation and self-assembly.[11,13] Such mesoscopic structures can enhance the uptake, repartitioning, and reactivity of metallic salts and acids.[14−18] Meanwhile, the uptake of inorganic components may increase the segregation regime.[19]

In this respect, an interesting class of materials is amphipolar arborescent copolymers with a core−shell−corona (CSC) architecture. Specifically, arborescent polystyrene-*graft*-[poly-(2-vinylpyridine)-*block*-polystyrene] copolymers were synthesized and very briefly investigated earlier for the preparation of gold nanoparticles.[11] The synthesis of these polymeric scaffolds requires the functionalization of linear and branched polystyrene (PS) substrates with acetyl coupling sites and grafting with "living" anionic polystyrene-*block*-poly(2-vinyl-pyridine) chains.[7] The resulting amphipolar dendritic species have a covalently bonded, layered architecture with an inner poly(2-vinylpyridine) (P2VP) shell that can coordinate with metallic salts or acids such as tetrachloroauric acid (HAuCl$_4$). This architecture effectively corresponds to a reverse unimolecular micelle but also contains a hydrophobic core in this case (Figure 1a).

The expected unimolecular micelle structure of arborescent copolymers offers a more stable template for loading polar compounds than self-assembled block copolymer micelles, since it has no critical micelle concentration. The dynamic exchange of chains within the micellar structures with free chains in solution is suppressed in these unimolecular micelles, even under nonselective solvency conditions, while the PS shell provides solubility in low- to medium-polarity solvents. Aside

from their inherent stability, arborescent copolymers offer important advantages over other templating methods. For example, variations in the degree of polymerization of the side-chain building blocks and the number of grafting cycles (generations) can provide control over the characteristics of the templates (e.g., core size, chain mobility, stabilizing layer thickness) beyond the limits achievable through the self-assembly of block copolymer chains. This system is also appropriate to study how the increase in radial density with generation affects the lateral segregation of the outer shell.

Here, we report on the discovery of unique phase segregation characteristics upon coordination of a class of amphipolar CSC arborescent copolymers with metallic salts or acids, including intramolecular nanodomain formation with morphologies resembling their block copolymer analogues, as well as new intricate structures. Additionally, to the best of our knowledge, there are currently no reports on intramolecular phase segregation to the extent observed for the CSC arborescent copolymers. To complete our research, we also performed computer simulations of arborescent copolymers in various solvents and after loading with metal salts to define the mesostructures of the obtained macromolecular objects and thus to better understand how the internal structure varies with the generation number, including the loss of radial symmetry through attractive interactions in the inner shell.

■ EXPERIMENTAL SECTION

Synthesis and Characteristics. A comprehensive investigation of the synthesis and the purification of the arborescent CSC copolymers serving as metallic nanoparticle templates in the current study was reported in ref 7. The compositional characteristics of the polystyrene substrates and the resulting CSC copolymers are

summarized in Tables 1 and 2, respectively, while the characteristics of the PS-*b*-P2VP block copolymers used in their synthesis can be

Table 1. Characteristics of Polystyrene Substrates Used in the Synthesis of CSC Copolymers

substrate	F^a	M_w/M_n	$M_w{}^b$	$f_w{}^c$
linear	0.26	1.06	6120	
G0PS	0.28	1.09	1.1×10^5	19
G1PS-1	0.30	1.11	9.3×10^5	136
G1PS-2^d	0.30	1.07	9.3×10^5	170
G2PS	0.22	1.09	1.2×10^7	1900
G3PS	0.26	1.08	2.2×10^7	2930

^{a}Functionalization (mol %) from ^{1}H NMR analysis. ^{b}Absolute values from size exclusion chromatography (SEC)-multiangle light-scattering (MALS) or laser light-scattering measurements before functionalization. ^{c}Branching functionality: number of branches added in the last grafting cycle. ^{d}Functionalized with chloromethyl groups.

Table 2. Characteristics of Arborescent CSC Copolymers

description	$M_w{}^a$	M_w/M_n	$f_w{}^b$	% 2VP^c
PS-*g*-(P2VP16-*b*-PS12)	3.4×10^5	1.06	12	52
G0PS-*g*-(P2VP11-*b*-PS8)	3.1×10^6	1.10	160	73
G1PS-*g*-(P2VP7-*b*-PS7)^d	8.3×10^6	1.03	529	33
G1PS-*g*-(P2VP15-*b*-PS11)^e	1.9×10^7	1.03	708	75
G1PS-*g*-(P2VP30-*b*-PS20)^e	1.7×10^7	1.05	319	62
G2PS-*g*-(P2VP7-*b*-PS13)	3.1×10^7	1.03	985	46
G2PS-*g*-(P2VP14-*b*-PS12)	3.9×10^7	1.02	1040	65
G2PS-*g*-(P2VP12-*b*-PS22)	3.7×10^7	1.01	750	55
G3PS-*g*-(P2VP14-*b*-PS12)	6.9×10^7	1.03	1850	70

^{a}Absolute values from SEC-MALLS or laser light-scattering measurements. ^{b}Branching functionality: number of branches added in the last grafting cycle. ^{c}mol %, from ^{1}H NMR analysis. ^{d}From substrate G1PS-1. ^{e}From substrate G1PS-2, all other substrates contained acetyl functional groups.

found in Table S3 (Section S2.1, Supporting Information). Additional characterization results for the arborescent copolymers, including representative size exclusion chromatography traces, can be found in Section S2.2, Supporting Information.

Metal Loading and Reduction. *Solution Loading.* The solvents used were toluene (EMD, Omnisolv), tetrahydrofuran (THF; EMD, Omnisolv), and chloroform (CHCl$_3$; Sigma-Aldrich, CHROMA-SOLV, for high-performance liquid chromatography (HPLC), ≥99.8%, with 0.5−1.0% ethanol as stabilizer). The template polymer was dissolved in the selected solvent at a concentration ranging from 0.1 to 0.5% w/v. Two different solution loading protocols were investigated: direct addition of the metallic salt or acid in the solid form to the polymer solution, or addition as a 1% w/v solution in the same solvent. For example, when loading was performed in toluene, solid HAuCl$_4$ was added, as it is not soluble in toluene, while in experiments using THF, gold was added as a THF solution. The template loading levels ranged from 0.125 to 1.0 equiv of metal per 2-vinylpyridine (2VP) unit. The polymer solutions were allowed to equilibrate with magnetic stirring for at least 24 h before analysis unless time-dependent experiments were performed. The metallic compounds investigated were tetrachloroauric acid (HAuCl$_4$; Alfa Aesar, 99.9%), palladium(II) acetate (Pd(OAc)$_2$; Strem Chemicals, min. 98%), and hexachloroplatinic(IV) acid (H$_2$PtCl$_6$; Sigma-Aldrich, ACS reagent).

Film Loading. The film-loading technique involved the deposition of an ionized copolymer solution and loading of the dry film by exposure to a solution of HAuCl$_4$. The arborescent copolymers were ionized by dissolution in THF (1.0% w/v, 10 mg/mL) and the addition of 1 equiv of HCl (Fisher brand, reagent grade, 12.0 N) per 2VP unit (HCl/2VP unit ratio = 1.0) with vigorous stirring. The

concentration of the HCl solution was varied for each copolymer composition to maintain a final solution composition of 98% v/v THF and 2% v/v water.

Thin films were cast from these solutions onto transmission electron microscopy (TEM) grids or atomic force microscopy (AFM) substrates, as described later in this section. Once the polymer film was dry, 1.0% w/v HAuCl$_4$ solution in Milli-Q water was placed on top of the film with a syringe and a 22-gauge needle (a single drop for the TEM grid, and multiple drops for the AFM films due to their much higher surface area, namely, 0.8 mm^2 vs 1 cm^2). The solution was left on the surface for 1 min for the TEM films and for 5 min for the AFM films and then wicked away with filter paper while holding the substrate with fine-tipped forceps. The films were rinsed by gently dropping Milli-Q water onto their surface with a syringe, and the remaining water droplets were wicked away with filter paper and blow-dried with a gentle stream of filtered air. The films were left to dry overnight before analysis.

Solution Reduction. Anhydrous hydrazine was prepared by vacuum thermolysis of hydrazonium cyanurate by a method adapted from Nachbaur and Leiseder.[20] Glass wool was placed loosely at the bottom of a 4.0 cm diameter glass tube terminated with a ground glass joint. The tube was connected to a finger condenser with a vacuum pump and a nitrogen purging line (see Appendix S1 (Supporting Information) for the reaction scheme and the apparatus used). The apparatus was evacuated and flamed to remove adsorbed moisture and then purged with nitrogen. The cylindrical glass tube was disassembled while purging with nitrogen, and hydrazine cyanurate (Fluka, 99+%) was loaded within the glass wool fibers. The tube was reattached to the condenser and placed in a horizontal tube furnace (Lindberg Heavy Duty, type 54032). After evacuation to 0.1 mm Hg, the sample was dried at 110 °C for 1 h. The temperature was then increased to 220 °C at a rate of approximately 2 °C/min, while the finger condenser was placed in a Dewar flask containing liquid nitrogen. The anhydrous hydrazine collected was transferred to a vial under nitrogen. The sealed vial was stored and used in a dry box. It should be noted that hydrazine is a highly toxic compound and is unstable, especially in the anhydrous form.

Solution reduction with anhydrous hydrazine (0.02% v/v in dry toluene) was performed in two different regimes, i.e., nearly stoichiometric conditions (1.2:1) and with a large excess (10:1) of N$_2$H$_4$/Au. The calculated amounts of hydrazine solution were added to the HAuCl$_4$-loaded templates. Following a loading time of at least 24 h, excess hydrazine was quenched by addition of an equimolar amount of concentrated HCl. The samples were then removed from the glovebox for centrifugation (1300*g*, 10 min), and films were cast from the supernatant.

A sodium borohydride (NaBH$_4$; Sigma-Aldrich, 98%) solution in methanol (0.5% w/v, 5 mg/mL) was prepared immediately before use and was added in a 10:1 ratio relative to the metal. The reducing reagent was added directly to the copolymer solution with vigorous stirring.

Solid-State Reduction. Ultraviolet Light Irradiation. Reduction of the HAuCl$_4$-loaded arborescent copolymers by UV irradiation used low-pressure mercury lamps (Rayonet photochemical reactor lamp, no. RPR-2537A) for 12 h at a distance of approximately 5 cm from the sample films cast on AFM or TEM substrates.

Plasma Treatment. HAuCl$_4$-loaded polymer samples were subjected to hydrogen plasma to both reduce the metallic salt and remove the polymer template in one step. A PVA TePla 100 plasma system was used to create a 200 W hydrogen plasma, and the samples (thin films cast on AFM or TEM substrates) were exposed for 60 min at 0.879 mbar H$_2$.

Hydrazine Vapor. HAuCl$_4$-loaded arborescent copolymer films cast on AFM or TEM substrates were placed in a vacuum line manifold also housing a small vial of anhydrous hydrazine. The manifold was purged with nitrogen and then partly evacuated to approximately 5 mm Hg. The system was isolated from the vacuum, and the hydrazine vapor was allowed to diffuse and react with the metal-loaded polymer films for 12 h.

Sodium Borohydride Film Reduction. Arborescent copolymers were loaded in solution with $HAuCl_4$ and then cast onto TEM grids. One drop of freshly prepared $NaBH_4$ solution in methanol (1.0% w/v, 10 mg/mL) was placed on top of the film using a syringe with a 22-gauge needle. The solution was left on the surface for 1 min and wicked away with filter paper, and the surface was gently rinsed with Milli-Q water. The remaining water droplets were wicked away with filter paper, and the film was blow-dried with a gentle stream of filtered air. The films were left to dry overnight before analysis.

Dynamic Light Scattering. Batchwise light-scattering measurements were carried out on a Brookhaven BI-200 SM light-scattering goniometer equipped with a BI-2030AT 201-channel correlator and a Claire Lasers CLAS2-660-140C (120 mW) laser operating at 656 nm. All of the samples were measured at 25 °C after at least three filtrations with a 0.45 μm poly(tetrafluoroethylene) (PTFE) membrane filter. The correlator was operated in the exponential sampling mode. The hydrodynamic radii were calculated from the *z*-average translational diffusion coefficients obtained from first- and second-order cumulant analyses of the correlation function (to better account for polydispersity effects) at a scattering angle of 90°. The solutions were prepared at concentrations ranging from 0.05 to 2.5%, depending on the molecular weight of the sample. The uncertainties reported on the radii measurements correspond to the standard deviation for a series of at least 10 measurements.

Transmission Electron Microscopy (TEM). *Thin-Film Preparation.* Thin films were cast onto 300-mesh copper TEM grids coated with carbon and Formvar (Electron Microscopy Sciences, FCF300-CU). When film treatment was required (metal loading, film reduction, UV, plasma), silicon monoxide-coated copper grids were used (Electron Microscopy Sciences, SF400-CU) due to their higher stability. The thin films were obtained by placing a drop of the polymer solution (0.1−0.5% w/v) onto the grid atop a piece of filter paper. The filter paper acted as a wicking agent to remove excess fluid and allow the formation of a thin film. The grid was then immediately transferred onto a fresh piece of filter paper and placed in a Petri dish for drying overnight under ambient conditions.

Instrumentation and Analysis Methods. The metal-loaded polymer films were imaged with a Philips CM10 TEM instrument operating at 60 kV. The images were recorded with an Advance Microscopy Techniques 11 megapixel digital camera and the accompanying Image Capture Software Engine version 5.42.558. Feature size analysis was performed with ImageJ processing software[21] by setting the scale for each digital image (pixels/nm) on the basis of the magnification and the resolution used. Feature size measurement was carried out by two methods. Samples not subjected to reduction were measured manually using the circle area function. Each feature was delimited by a manually drawn circle whose area was determined by the software, and the effective radius was calculated from the area. At least 30 measurements were recorded for each sample to provide adequate size distribution information. For the reduced samples, the features were well-defined and had high contrast with the background, and thus the automatic analysis tool (Analyze Particles) was used. This tool measures the area of all particles within the limits of a user-defined circular threshold, which encompassed the individual metallic regions. This process typically yielded at least 300 area measurements from which the radii and size distribution were calculated.

In some cases, a high pass filter was applied to the TEM micrographs with photoediting software, to correct for uneven exposure and allow for better visualization and more accurate measurement of the features.

Scanning Electron Microscopy (SEM). Scanning electron microscopy (SEM) was performed with a Hitachi model S2000N instrument at voltages ranging from 3 to 15 kV and working distances from 5 to 10 mm in the field emission mode (FE-SEM). Samples analyzed by SEM were prepared on silicon substrates as described below.

Atomic Force Microscopy (AFM). *Substrate Preparation and Film Casting.* Muscovite mica sheets cut into 1 cm^2 pieces were adhered to a steel substrate of approximately the same size using double-sided tape, to allow securing of the sample to the magnetic

spin coater and the magnetic scanner head of the AFM instrument. Immediately prior to film casting, the mica was cleaved with a strip of tape (Scotch Magic brand tape) to expose a fresh (hydrophilic) surface.

Silicon substrates were also used after cleaning and activation immediately prior to film casting. A silicon wafer was cleaved into 1 cm^2 pieces with a diamond knife, cleaned in an ultrasonic bath with 2-propanol for 3 min, and then blown dry with filtered nitrogen. The wafers were then exposed to UV light (5 mW/cm^2, 40 W, UV Technik Speciallampen GmbH, main emission 185 nm) and ozone for 12 min at an oxygen flow of 500 mL/min. Acidic etching was also used to clean and activate the silicon when the UV/ozone apparatus was not available. This was performed by immersion of the substrate in a solution of sulfuric acid and hydrogen peroxide (30%) 3:1, followed by water, acetone, methanol, and 2-propanol rinses. The substrates were dried with a stream of filtered nitrogen and fixed to a metal substrate using double-sided tape.

After mounting on the magnetic spin coater, drops of solution were placed on the substrate with a pipette to completely cover it and the substrate was spun for at least 15 s at 3000 rpm.

Instrumentation and Analysis Methods. AFM images were recorded in the tapping mode on a Nanoscope III SFM instrument (Digital Instruments, model MMAFM-2, scan stage J) housed in a NanoCube acoustic isolation cabinet/enclosure mounted on a Halcyonics Micro 40 vibration isolation table. The measurements were performed under ambient conditions using Si probes (VistaProbes T300) having a spring constant of 40 N/m, a resonance frequency of 300 kHz, and the following characteristics: length 125 μm, width 40 μm, tip height 14 μm, and tip radius <10 nm. The images were captured and analyzed using Nanoscope v5.30r3.sr4 software.

Images were recorded at a maximum scan rate of 1 Hz while simultaneously acquiring height and phase information. Set-point amplitudes were sample-dependent, ranging from 0.85 for hard-tapping and 0.50 for light-tapping conditions. Typical feedback control settings were as follows: integral gain 0.20, proportional gain 2.0, and scan angle 0. Feature size was determined by power spectral density (PSD) analysis,[22−24] with uncertainties representing the standard deviation on multiple PSD analyses, or by manual measurement using the software.

Optical Microscopy. The films cast for the AFM studies of film-loaded species were examined for substrate adhesion with a Zeiss Axioplan optical reflection microscope equipped with a differential interference contrast (DIC) module. The microscope was equipped with a Zeiss Axio Cam MR digital camera for image acquisition.

UV−Vis Spectroscopy. Absorption spectra were acquired on a CARY 100 Bio UV−vis spectrophotometer with Cary Varian UV scan application (v3.001339). A quartz cell with a 1 cm path length was used to measure the absorption for metal-loaded polymer solutions at a concentration of ca. 0.02 mg/mL.

Ellipsometry. Layer thicknesses for thin polymer films to be analyzed by AFM were determined using an MM-SPEL-VIS ellipsometer from OMT. Each film was prepared by spin-casting at 2500 rpm from a polymer solution concentration of 0.2% w/v (2 mg/mL). The silicon substrates were examined with a spectral method in the wavelength range from 450 to 900 nm, while the azimuthal angle was set to 15°. Sample position is paramount for consistent measurement of film thickness and can result in systematic errors due to variations in the angle of incidence and the azimuthal angle. Errors were minimized by measuring all of the samples in one measurement session to ensure that the geometry of the device and the sample holder position remained the same. Each measurement was recorded over an average area of 3 × 5 mm^2. A bare, newly cleaned silicon substrate was also measured to correct for the oxide layer thickness. Each sample was measured three times in different areas, resulting in film thickness variations of less than 1 nm in all cases.

Table 3. DPD Interaction Parameters (in Units of $k_B T/r_c$) Used in the Simulations[a]

a_{ij} (χ_{ij})	A	B	S1	S2	S3	M
A	25	39.5 (2.92)	28.6 (1.11)	26.1 (0.32)	26.1 (0.32)	40
B	39.5 (2.92)	25	26.5 (0.45)	37.8 (3.90)	30.6 (1.72)	25
S1	28.6 (1.11)	26.5 (0.45)	25			
S2	26.1 (0.32)	37.8 (3.90)	[b]	25		45
S3	26.1 (0.32)	30.6 (1.72)			25	40
M	40	25		45	35	40

[a]The numbers in brackets in the nondiagonal cells are the corresponding values of the Flory–Huggins parameter. [b]The interactions that were not considered both in experiments and in simulations.

COMPUTER SIMULATIONS

Method. Dissipative particle dynamics (DPD) simulations[25,26] were used to study the behavior of arborescent copolymers in various solvents as in our previous work.[27] In this mesoscopic method, all solvent molecules and polymer segments are explicitly included and represented in terms of beads of equal mass m, whereby each bead usually comprises a group of atoms. The beads interact with each other by a pairwise additive force

$$\mathbf{F}_i = \sum_{i \neq j} (\mathbf{F}_{ij}^C + \mathbf{F}_{ij}^D + \mathbf{F}_{ij}^R + \mathbf{F}_{ij}^B) \tag{1}$$

where $\mathbf{F}_{ij}^C$ is a conservative force responsible for repulsion via soft potential characterized by the parameter a_{ij}[6]: the larger the value of a_{ij}, the stronger the repulsion between the ith and the jth bead. $\mathbf{F}_{ij}^D$ and $\mathbf{F}_{ij}^R$ are the dissipative and random forces, respectively, which serve as heat sink and source and are specified by a friction coefficient λ and the noise amplitude σ. $\mathbf{F}_{ij}^B$ is a bond force that keeps the polymer beads together and that is specified by the spring constant k_s and the equilibrium bond length r_0. The sum runs among all of the beads in the system. The first three forces in the right-hand-side of eq 1 act only within a certain cutoff radius r_c, which usually serves as the characteristic length-scale unit.[26] Additional description can be found in the Supporting Information.

Coarse-Graining. Before the arborescent CSC copolymer models can be constructed, so that the experimental and simulation results can be compared, the simulation parameters should be first related to the physical time and space scales. We start with the determination of the characteristic length r_c, defined as $r_c = (\rho V_{DPD})^{1/3}$, where ρ is the number density set to 3, and V_{DPD} is the volume of a single DPD bead. In the current simulations, there were two main types of beads, A and B, representing the monomer units of polystyrene (PS) and poly(2-vinylpyridine) (P2VP), respectively. Since the volumes of the single monomers are on the same order (161.03 vs 153.50 Å³ for PS and P2VP, respectively[28]), one can select a V_{DPD}, which would allow both to include integer numbers of PS or P2VP monomers N_m into one DPD bead and to model the coarse-grained polymer branches as flexible ones. Following the work of Posocco et al.,[28,29] the N_m was set to 5, and the resulting groups of PS and P2VP monomers had volumes of 805.15 and 767.5 Å³, respectively. By selecting the V_{DPD} as the mean value, $V_{DPD} = 787$ Å³, $r_c = 1.33$ nm was obtained, which is close to the persistence length of atactic polystyrene.[30] Thus, the values for A–A, B–B, and A–B bonds were selected as for flexible chains, namely, $k_s = 20$ and $r_0 = 0.7$. Simultaneously, with such a V_{DPD}, the beads have a mass of 520 Da (520 g/mol), and thus the time unit τ could now be

determined (see the previous paragraph). As a result, at $T = 298.15$ K, $\tau = 19.3$ ps was obtained.

The next step in the coarse-graining procedure was in the determination of interactions among polymers, solvents, and the metal salt. Since $\rho = 3$, the interaction parameters a_{ij} (in units of $k_B T/r_c$) can be mapped onto the Flory–Huggins parameters χ_{ij} using a linear relation[26]

$$a_{ij} \approx a_{ii} + 3.27 \chi_{ij} \tag{2}$$

where $a_{ii} = 25$ for any two beads of the same type. In turn, the calculation of Flory–Huggins parameters can be done through the Hansen solubility parameter (HSPs)[31]

$$\chi_{ij} = \frac{\alpha V_{DPD}((\delta_i^d - \delta_j^d)^2 + 0.25(\delta_i^p - \delta_j^p)^2 + 0.25(\delta_i^h - \delta_j^h)^2)}{k_B T} \tag{3}$$

where α is a numerical coefficient usually taken as 0.6,[32] and δ^d, δ^p, and δ^h are the dispersion, polar, and hydrogen-bonding Hansen solubility parameters (HSPs), respectively.

In the current simulations, restricted to the case of arborescent copolymers in three solvents, namely, THF, toluene, and CHCl₃, the corresponding interactions between the polymer and solvent DPD beads of types S1, S2, and S3, respectively, were considered. In addition, since only the case of HAuCl₄ loading in toluene and CHCl₃ was considered, corresponding metal salt beads were introduced of type M. The values of HSP for the polymers and the selected solvents, obtained from existing data,[31,33] are summarized in Table S1.

Then, according to eqs 2 and 3 at $T = 298.15$ K, one can obtain the DPD repulsion parameters a_{ij} together with the Flory–Huggins parameters. To account for the effect of blockiness of the CSC copolymers on the PS–P2VP interactions, the corresponding a_{AB} parameter was calculated from the additional relationship proposed by Glotzer et al.[34]

$$a_{AB} = a_{AB} + 3.27 \left(1 + \frac{3.9}{N_{DPD}^{0.51}}\right) \chi_{AB} \tag{4}$$

where N_{DPD} is the length of the diblock graft. Here, $N_{DPD} = 52$, which was selected as the mean value among all of the lengths of grafts for the arborescent macromolecules considered (see Table S3). The resulting set of simulation parameters is provided in Table 3. As can be seen, on this coarse-grain level, all of the solvents act like selective ones, while PS and P2VP are strongly incompatible. THF appears to be the least selective solvent, while maximum selectivity is observed for toluene.

Finally, to determine the interactions of the HAuCl₄ molecules with the polymers and the solvents, the approach proposed recently by Santo et al.[35] was used. Briefly, it was assumed that the mutual repulsion between M beads was

stronger than between the rest of the substances (a_{MM} = 40). Next, the following facts obtained from the literature[29,36] were taken into account, namely, that HAuCl$_4$ molecules create complexes only with P2VP monomers and that they are poorly soluble in toluene and only slightly soluble in CHCl$_3$. The set of corresponding parameters is also presented in Table 3.

Models. *Arborescent Copolymers.* The models for the macromolecules were designed in the same way as in our previous work[27] and taking into consideration the synthetic protocol actually used.[7,11] Initially, linear chains of type A are grafted onto a linear chain substrate of the same type, and thus a G0 macromolecule is obtained. Then, considering the grafted chains (branches) as the precursors, the subsequent linear chains are grafted onto them to obtain the arborescent polymer of first generation. Repeating the same grafting procedure with branches of the last generation, highly branched polymers of up to the fourth generation were constructed. To obtain the CSC copolymers, AB diblock copolymers were grafted in the last grafting cycle through the free end of type B.

One of the main goals in the construction of models for both the arborescent homopolymer substrates and the copolymers was to achieve the same molecular weight M_w and branching functionality f_w of the macromolecules used in the experiments. Considering the length and the mass scale used in the simulations (see the previous paragraph), the length of each graft PS chain was set equal to 10 beads (M_w = 5200 g/mol), except for the linear substrate, which had 11 beads (M_w = 5720 g/mol) to correspond with the experimental samples (see Table 1). It was also assumed that acetyl or chloromethyl coupling sites were part of the substrate branches. In turn, the length of the AB grafts was the same within one generation but different for each CSC sample (see Table S3).

The total number of grafts varied for the different generations, while it was set constant for all types of PS substrates (e.g., the total number of PS grafts in the G1 molecules was considered to be the same for G1PS-1, G2PS, and G3PS substrates). In other words, the number of grafts per branch (or the grafting density) for each generation also varied. To gain a better understanding of the construction algorithm, let us consider the case of G1PS-g-(P2VP7-b-PS7). First, one needs to obtain f_w = 137 for a G1PS-1 substrate. To this end, one may graft 19 chains of 10 beads each onto the linear substrate and then graft approximately 7.2 chains of the same lengths onto each G0PS branch. This means that about 80% of the branches have seven grafts, while the remaining branches have eight grafts. Following the same logic, to obtain the corresponding CSC copolymer, one may add 3.87 grafts onto each current substrate branch, i.e., either 3 or 4 AB copolymer chains with 27 beads (13 beads of type A and 14 beads of type B). As a result, an arborescent copolymer model with $M_w \approx$ 8.26 × 10^6 and f_w = 530 is constructed.

Finally, it was assumed that the grafts on each branch were distributed homogeneously for each generation. The resulting characteristics of the arborescent copolymer models obtained (including the length of the AB copolymer grafts), together with the arborescent PS substrates, are summarized in Table S2. For comparison, the table also includes the experimentally determined values of molecular weights M_w^{exp} and branching functionalities f_w^{exp} of the corresponding samples. While most values of M_w and f_w for the coarse-grained models appear to be in close agreement with the values obtained from SEC-MALLS or laser light-scattering measurements, a larger deviation in weight is observed for G3PS-g-(P2VP14-b-PS12). This may be

due to the assumption of the equality of the lengths of the PS grafts in the substrates (Table S2).

HAuCl$_4$ Loading. For simplicity, the metal salt loading of arborescent copolymers in simulations is considered as the instantaneous functionalization of P2VP domains by beads of type M. In other words, single beads of type M are randomly grafted simultaneously onto the B beads and maintained near them by a bonding force $\mathbf{F}_{ij}^B$ with the following parameters: k_s = 100 and r_0 = 0.1. Such values were selected to account for the high binding energy of the HAuCl$_4$−2VP complex.[36] In relation to the coarse-grained level selected, the amount of metal salt beads needed to coordinate a certain (equivalent) amount of P2VP segments can be estimated. Because the molar mass of each DPD bead was ~520 g/mol and the molar mass of the HAuCl$_4$ molecule was ~339 g/mol, each M bead represented 1.5 metal salt molecules. Meanwhile, each P2VP bead contains five monomers (see the previous paragraph). Consequently, to coordinate every second 2VP unit in the CSC copolymers containing N P2VP coarse-grained beads (0.5 equiv), the macromolecules were loaded with 1.667N beads of type M.

Simulation Systems. All of the simulations were performed using open source software LAMMPS,[37] with an integration time step $\Delta t = 0.02\tau$, where τ is the characteristic time scale. Initially, single macromolecules were modeled in a solvent (either of type S1, S2, or S3) in cubic simulation boxes with imposed periodic boundary conditions. The dimensions of the boxes varied from $L_x \times L_y \times L_z = 24r_c \times 24r_c \times 24r_c$ to $L_x \times L_y \times L_z = 100r_c \times 100r_c \times 100r_c$, depending on the generation of the arborescent polymer. In addition, to study the aggregation behavior in toluene solutions of PS-g-(P2VP16-b-PS12) samples, 100 copolymer molecules were placed in a cubic box with dimensions $L_x \times L_y \times L_z = 80r_c \times 80r_c \times 80r_c$. Equilibration of the systems was allowed over 5 × 10^6 steps. The size of the single macromolecules was then estimated as their hydrodynamic radius r_{DPD} based on snapshots taken every 25 × 10^3 steps over 1 × 10^6 additional steps. The value of r_{DPD} was determined for homogeneous hard spheres (similar to polymer microgels),[38] $r_{DPD} = \sqrt{5/3}\, r_g$, where the radius of gyration r_g was calculated from the following formula:[27]

$$r_g^{\,2} = \frac{1}{2A^2} \sum_{i,j}^{A} \langle (x_i - x_j)^2 + (y_i - y_j)^2 + (z_i - z_j)^2 \rangle \tag{5}$$

where A is the total number of DPD beads in the arborescent (co)polymer.

After equilibration, the CSC copolymers were functionalized with metal salt beads and allowed to equilibrate further in the solvent from 2 × 10^6 to 10 × 10^6 steps, depending on the generation.

RESULTS AND DISCUSSION

Solution Behavior of CSC Copolymers. Since metallic salt coordination alters the properties of arborescent copolymers, we started with a study of branched (template) polymers in solution, which allowed us to provide a comparison with the case of intermolecular micelles. Major attention was given to the characteristics of the copolymers in toluene because the metal-loading studies were carried out in this solvent for comparison with intermolecular micelles of PS-b-P2VP. The size of the macromolecules was measured with
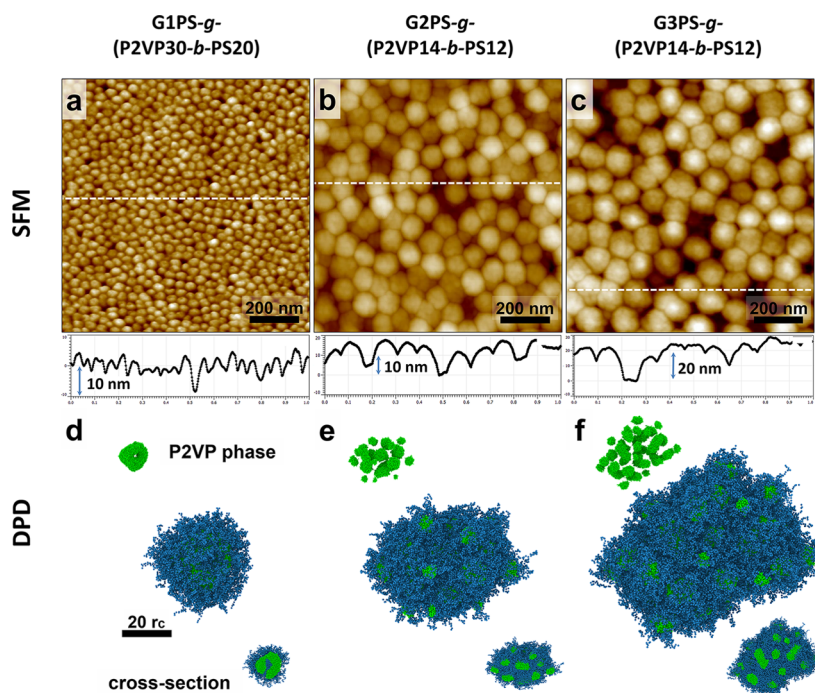
Figure 2. SFM height images and corresponding height profiles along the horizontal lines (a−c) for copolymers cast from toluene solution, and simulation snapshots in a selective solvent (d−f): (a, d) G1PS-*g*-(P2VP30-*b*-PS20), (b, e) G2PS-*g*-(P2VP14-*b*-PS12), and (c, f) G3PS-*g*-(P2VP14-*b*-PS12). The scale bar of all of the SFM images is 200 nm. In the snapshots, the green beads represent the P2VP segments, while the blue beads represent the PS segments. The upper row of smaller images depicts only the P2VP phase, while the lower row of images depicts cross sections through the center of mass.

dynamic light scattering (DLS). To assess the aggregation tendency, the hydrodynamic radii for first- and second-order analyses of the autocorrelation functions r_{h1} and r_{h2} were evaluated. In turn, the difference between r_{h1} and r_{h2} provides this information—the larger the difference, the greater the aggregation tendency. In addition, irreproducible radii in successive measurements, leading to large standard deviations, can indicate the presence of poorly defined aggregates with broad size distributions. The first- and second-order hydrodynamic radii determined in toluene from the autocorrelation function are summarized in Table S4 for both the polystyrene substrates and the CSC copolymers. The table also includes the hydrodynamic radii r_{DPD} obtained from DPD simulations and the scanning force microscopy (SFM) measurements. Finally, the molecular dimensions of arborescent (co-)polymers in various solvents are compared in Table S5.

The results show that all of the template polymers appear to be essentially monodisperse in solution, with the exception of the G0 copolymer, PS-*g*-(P2VP16-*b*-PS12). This is evident from the excellent agreement between the first- and second-order analysis results of the correlation function and the consistent values obtained, as indicated by the small standard deviations. The G0 copolymer, in contrast, has a significant discrepancy between r_{h1} and r_{h2}, even though the standard deviation on the measurements is comparable to the other samples. On the contrary, no discrepancy was found in the less selective solvents, namely, tetrahydrofuran (THF) and chloroform (Table S6). This may indicate aggregation of the branched macromolecules into clusters. To prove this, we simulated a solution of G0 copolymers and plotted the aggregation number histogram[27] (Figure S3). It can be seen that a majority of the copolymer molecules (about 70%) form clusters, and the mean aggregation number equals two.

Therefore, it may be assumed that the value of r_{h1} corresponds to dimers of the CSC copolymers, while r_{h2} is closer to the dimensions of single macromolecules.

Furthermore, the molecular characteristics of the arborescent polystyrene substrates and the corresponding copolymers can be summarized with a scaling relation for the size of the arborescent polymer generations with molecular weight having a scaling exponent of 0.32 (Figure 1b), which is in accordance with a previous report asserting that arborescent structures have a spherical symmetry and a high segment density.[39] Interestingly, while the scaling exponent obtained in simulations had a similar value, the absolute values of r_{DPD} of the CSC copolymers were almost half of the hydrodynamic radii obtained from DLS analysis. These values are also closer to the ones calculated for the dry molecules and the bulk radii calculated based on the composition determined by ^{1}H NMR spectroscopy (Table S6). These variations may due to differences in the methods used to determine r_h (top-down vs bottom-up) and to the assumption that the grafts were distributed homogeneously within the substrate branches for all of the generations. Since the arborescent PS substrates were constructed from relatively short (5000 g/mol) PS chains and the core dimensions were comparable to the side chains, we may expect that the studied macromolecules possess spherical symmetry. It was previously shown that arborescent homopolymers of higher generations behave like rigid spheres in solution,[40] while transfer to a solid substrate yields monomolecular films of weakly deformed particles.[41] Regarding the current CSC copolymers, we may expect that the hard sphere behavior may suppress intermolecular interactions regardless of solvent selectivity, as well as give rise to peculiarities in intramolecular interactions. To examine such features, analogous SFM measurements were done with
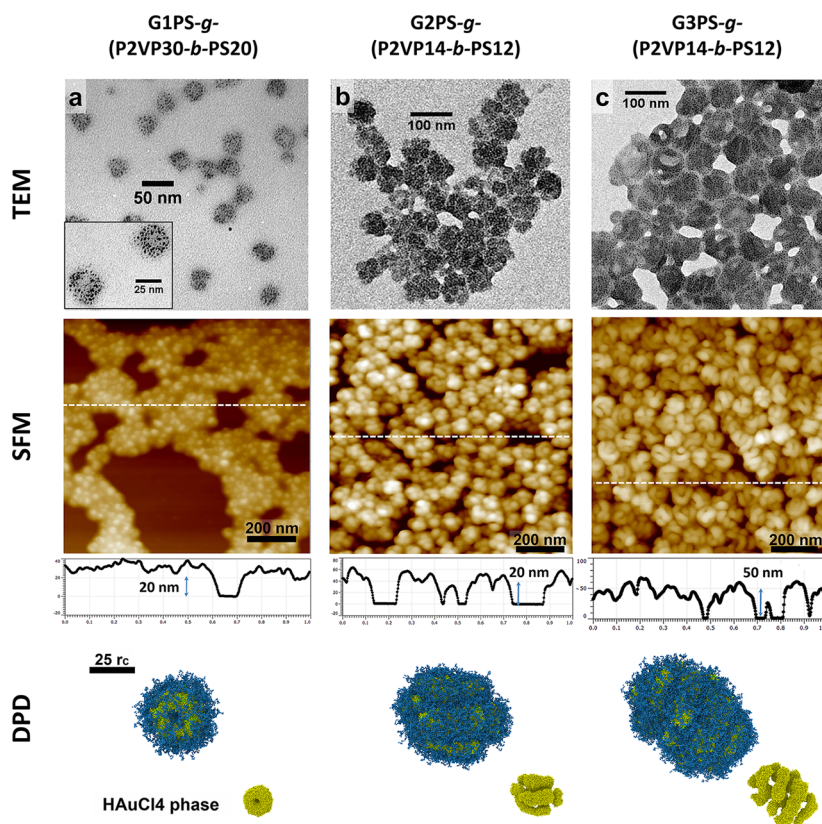
Figure 3. TEM micrographs (upper row), SFM height images (middle row), and DPD simulation snapshots (lower row) for arborescent CSC templates loaded with 0.5 equiv. of HAuCl₄/2VP unit in toluene: (a) G1PS-*g*-(P2VP30-*b*-PS20), (b) G2PS-*g*-(P2VP14-*b*-PS12), and (c) G3PS-*g*-(P2VP14-*b*-PS12). For the G1PS-*g*-(P2VP30-*b*-PS20) TEM image, the black dots in the inset are ultrasmall Au clusters produced upon electron beam irradiation,[19] more visible at high magnification. The SFM images are presented with their respective height profiles along the lines. For all simulation snapshots, the smaller images depict only the HAuCl₄ phase.

arborescent copolymers having similar architectures but a different composition.[42] The height images acquired for generations G2–G4 of the arborescent copolymers cast from toluene solutions are provided in Figure 2a–c. The corresponding data for the full copolymer set from G0 to G4 can be found in Figure S4.

Several conclusions can be drawn from these results. First, it is evident that as the generation number increases, not only does the size increase as expected, but more importantly, the spherical structures are better-defined. This is attributed to the increased branching functionality yielding less interpenetrable structures, similar to branched homopolymers.[42] However, in the current case (PS and P2VP), preferential adsorption of the P2VP segments onto hydrophilic substrates can cause significant flattening of the structures.[43] This can be seen clearly for the lower generation (G0 and G1) species, which are more flexible (Figure S4a,b, respectively). On the contrary, for arborescent copolymers of higher generations, the height micrographs in Figures 2a–c and S4c–e show that the deformation of the branched macromolecules is limited, and each observable spherical entity is a single arborescent molecule with a fuzzy substructure. Therefore, in agreement with the DLS results, aggregation can be excluded for such polymers.

Second, the SFM images show the formation of weakly pronounced, yet still distinguishable, nanodomains within each of the G2–G4 arborescent CSC copolymers. While for the dry macromolecules this is the result of the high incompatibility of the PS and P2VP segments,[28,29] together with the fact that the

transition to the bulk state may induce microphase separation,[44] it should be clarified whether these nanodomains exist in the swollen copolymers, since the presence of the solvent should screen undesirable monomer–monomer interactions.[39] To answer this, DPD simulations were performed, and the corresponding simulation snapshots for single macromolecules swollen in a sufficiently selective solvent (toluene) are provided in Figures 2d–f and S4f–j. As can be seen, the snapshots reveal a good correlation with the SFM images. Solvent selectivity mediates phase separation, and the copolymers of lower generations adopt a core–shell or CSC morphology (Figure S4f,g) with continuous P2VP domains. For increasing generations and number of branches, however, the formation of single lyophobic domains becomes unfavorable. Otherwise, aggregation of an increasing number of branches would cause loss of conformational entropy for the swollen PS blocks. Thus, the radial symmetry is altered, and a reasonably distinct toroid morphology (Figure 2d) is observed for the G2 copolymer, while multicore (cauliflower-like) morphologies are seen for arborescent copolymers of higher generations (Figure 2e,f). Simultaneously, the morphologies in weakly selective solvents (THF and chloroform) display no clear phase boundary, in spite of the incompatibility between unlike polymer segments[29] (Figure S5b,c). The observed conformations are the result of swelling of both blocks in the solvents, which decreases the number of unfavorable PS–P2VP contacts in comparison with melts, thus preventing phase separation. Interestingly, the simulations also show that the break in radial symmetry makes the overall shape of

arborescent copolymers of higher generations (G3 and G4) deviate slightly from a perfect sphere. One may thus expect a small degree of asphericity for the branched copolymers studied in these experiments, while casting onto a solid surface (Figure 2a−c) and drying may cause collapse of the swollen PS branches and thus induce a spherical shape.

HAuCl$_4$ Loading. Having established the physical properties of the arborescent CSC templates, the study of coordination with HAuCl$_4$ could be considered, which was performed for the copolymers described in Table 2. As the metal selectively coordinates with the P2VP phase of the templates, the metal distribution should conform to the morphology of the arborescent CSC macromolecules. The metal repartition can be reconstructed using transmission electron microscopy (TEM) imaging.[45] Following dissolution of the arborescent copolymers and the addition of HAuCl$_4$, the polymer solution was allowed to equilibrate for 48 h to load 0.5 equiv of HAuCl$_4$ relative to the 2VP units. The results obtained for the G2−G4 templates are provided in Figure 3, while the results for lower generations are shown in Figure S6.

For the G0 and G1 templates, the TEM micrographs and the corresponding SFM height images both show a uniform distribution of Au clusters in a spherical morphology (Figure S6). Based on the dimensions, the structures were assigned to individual macromolecules. Indeed, the radii of the Au-rich regions, well-contrasted in TEM micrographs (Figure S6), were measured to be 9 ± 1 and 11 ± 1 nm for the PS-g-(P2VP16-b-PS12) and G0PS-g-(P2VP11-b-PS8) templates, respectively. SFM analysis (Figure S6) also confirmed the spherical morphology of the Au-loaded micelles, with mean heights of 28 ± 1 and 34 ± 1 nm for HAuCl$_4$-loaded PS-g-(P2VP16-b-PS12) and G0PS-g-(P2VP11-b-PS8), respectively. It should be noted that significant aggregation was observed for gold-loaded G0PS-g-(P2VP11-b-PS8) in DLS, which is in agreement with the observation of the gold-stained domains in the TEM images. This is attributed to the short PS chains in the corona (M_w = 8200 g/mol) being unable to shield the charged metallic salt-loaded cores in the apolar (toluene) environment, leading to molecular aggregation (yet, without interpenetration, Figure S6b).

Remarkably, distinct morphologies were discovered for the samples of higher generations. As demonstrated in Figure 3a, loading the G1PS-g-(P2VP30-b-PS20) sample with 0.5 equiv of HAuCl$_4$/2VP unit resulted in nanoscale metal organization within each template molecule. A nonuniform distribution of gold clusters could be observed since the periphery of the molecules was more densely loaded than the center. Thus, ringlike nanostructures with a radius of 15 ± 2 nm are present within the G2 templates. While some molecules display distinct radial gradation of the metal, complete ring structures are not observed in all cases.

It was postulated that ringlike and partial ringlike organizations of the metal within the arborescent templates resulted from flattening of the spherical metal-loaded structures upon transfer to the TEM grid. During film deposition, the long block copolymer chains may indeed collapse in a radial fashion, exposing the metal-depleted G1PS core. This hypothesis was confirmed by SFM analysis of a submolecular layer, where a distinct ringlike organization was evident in the height image (middle row in Figure 3a) and the corresponding DPD simulation snapshots (lower row in Figure 3a).

It therefore appears that metal uptake in the polymer scaffolds by coordination with the 2VP units induces intramolecular phase separation within each molecule in a process likely initiated by the selectivity of the solvent (Figure 3). Intramolecular phase separation yielded the toroidal polymer morphologies visualized by both TEM and SFM analyses of the dried samples on the substrate (the partial-toroid morphologies can be considered as the visualization of particles lying "on side") and in the DPD simulations in the bulk solvent. The toroidal nanostructures had a mean diameter of 22 ± 2 nm, in agreement with the TEM measurements. Coordination with the gold salt favors the intramolecular aggregations of P2VP grafts, which competes with the propensity of the arborescent core to maintain a uniform density. Such an interplay leads to this unique transition to nonspherical structures upon metal complexation, which is expected to depend on the generation number of the PS core. Subsequently, loading of the G3 and G4 templates with the Au salt revealed strikingly different morphologies (Figure 3b,c). For the G3 template, G2PS-g-(P2VP14-b-PS12), a raspberry or a sphere-in-sphere morphology was formed, whereby each template molecule segregated into multiple nodules within a spherical boundary, giving it a raspberry-like appearance observed in both TEM and SFM images. SFM provided a much clearer picture of the topology, as it probes the whole material and not only a two-dimensional projection of the metal-rich regions like TEM. According to SFM analysis, the nodules had a diameter of 25 ± 4 nm and were bound within a spherical volume with a radius of 34 ± 1 nm. The molecular boundaries defined by gold uptake had a radius of 33 ± 2 nm in the TEM images. Meanwhile, the simulation snapshots of the single salt-loaded molecules reveal a similar multicore morphology (Figure 3b). Since the size of the cores is considerably larger than observed for the unloaded copolymers (Figure 2b), we may assume that metal coordination also causes aggregation of the initially solvent-mediated intramolecular domains. While some aggregates have a rather cylindrical shape, this might be due to (a) the presence of solvents in the interior of the molecules, causing swelling and increasing the conformational entropy of the PS grafts, and (b) the assumed homogeneous distribution of grafts within each generation in the simulated macromolecules.

The morphology of the G4 template, G3PS-g-(P2VP14-b-PS12), is a seemingly continuous cylindrical structure coiled within the spherical boundary of each branched template molecule. The constraints imposed by the PS core, yielding phase-segregated wormlike domains localized within discrete spherical volumes reported herein, are the first of their kind for a single molecule system. The spherical volume constraining the cylindrical polymer segments of the arborescent system, shown in Figure 3c, has radii of 40 ± 2 and 39 ± 2 nm according to TEM and SFM analyses, respectively. The width of the cylinders measured by SFM imaging was 28 ± 3 nm, which is comparable within error limits with the nodule diameter measured for the G3 copolymer (25 ± 4 nm). The similar dimensions observed in both cases is attributed to the comparable length of the PS and P2VP segments in the block copolymers used to construct both templates. Finally, the simulation snapshots show the same morphology within single template molecules (Figure 3c), while the slightly aspherical shape of the particle is inherited from the initial CSC copolymer substrates (Figure 2c).
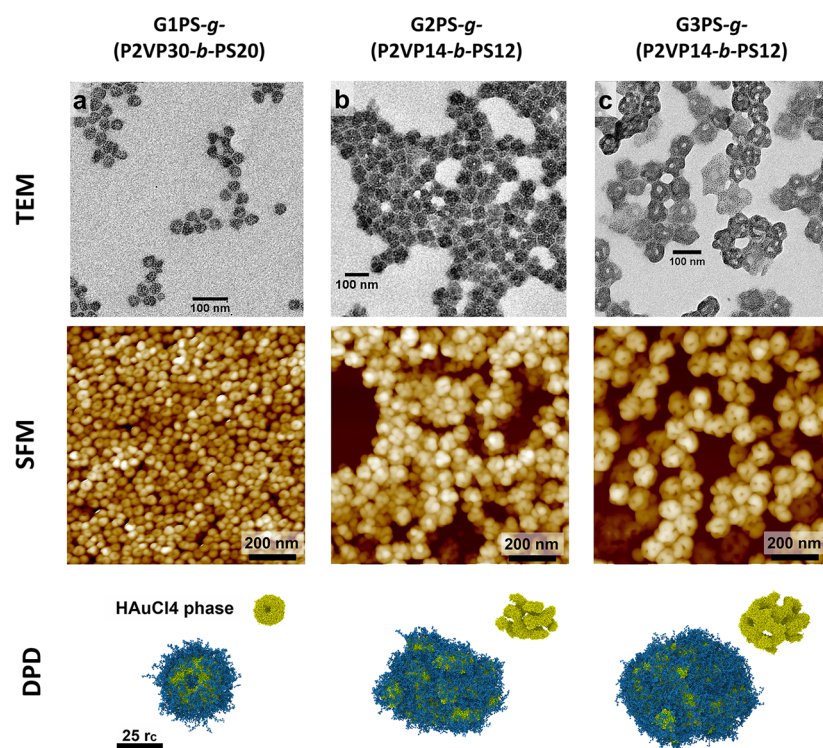
Figure 4. TEM (upper row) and SFM height (middle row) images and simulation snapshots for single macromolecules (right column) with 0.5 equiv of HAuCl$_4$/2VP unit in CHCl$_3$: (a) G1PS-*g*-(P2VP30-*b*-PS20), (b) G2PS-*g*-(P2VP14-*b*-PS12), and (c) G3PS-*g*-(P2VP14-*b*-PS12). For all simulation snapshots, the smaller images depict only the HAuCl$_4$ phase.

Overall, we may conclude that the resulting intramolecular structures emerged before deposition onto the substrates (in bulk solution) and should not be considered as resulting from molecule−surface interactions. It is also apparent that the loading level should have an influence on the overall morphology. This was also examined, and the results are provided in Section S2.4, Supporting Information (Figures S7−S9). The main conclusion drawn is that lowering the loading level leads to less defined nonspherical morphologies (Figure S7) although other important factors also need to be discussed.

Considering that the G3 and G4 templates discussed above have block copolymer side chains with nearly identical molecular weights and block length ratios, a relationship can be established between topological constraints and the morphology obtained after coordination with HAuCl$_4$. Since the side chains are nearly identical, our attention was drawn to the characteristics of the PS cores used as substrates (Tables 1 and S4). While the PS cores differ in terms of generation number (G2PS and G3PS for the G3 and G4 copolymers, respectively) and molecular weight by nearly 10^6 g/mol, their hydrodynamic radii are essentially identical (r_{h2} = 28−29 nm). This suggests that the G3PS substrate, being denser than G2PS, impacts the location of the grafted side chains. For a denser substrate, grafting should be favored on its periphery, as chain diffusion to coupling sites within their interior would be hindered by steric crowding. The peripheral grafting hypothesis is supported by the hydrodynamic dimensions of the copolymers. The G4 copolymer G3PS-*g*-(P2VP14-*b*-PS12) (r_{h2} = 75 ± 1 nm) is significantly larger than its G3 analogue G2PS-*g*-(P2VP14-*b*-PS12) (r_{h2} = 51 ± 1 nm), even though the substrates and the side chains have similar characteristics. With enhanced peripheral grafting, phase separation between the PS

substrate and the P2VP shell should be favored. A P2VP phase relatively devoid of substrate PS chains apparently has a greater tendency to form continuous wormlike domains in the G4 species. The G3 system, with more significant intermixing of the PS chains from the core, due to greater fluctuations in the position of the grafted side chains, would perturb the continuity of phase separation and produce nodular domains.

The influence of the side-chain length on morphology was also examined, and the results obtained are provided in the Supporting Information (Section S2.5 and Figure S10). The main conclusions drawn are that for the G2 CSC templates, nonspherical phase segregation is only observed if the length of the block copolymer chains is significantly larger than the length of the PS chains in the substrate, while for G3 templates, the morphologies appear to be independent of the length of the P2VP segments (at least within the range tested) and of the length of the PS segments in the corona for all of the samples considered (Figure S10).

Effect of Solvent on Morphology. As mentioned earlier, the morphology of intermolecular micelles is known to depend on different factors including the solvency conditions used. Solvent-quality variations thus represent a way to assess the stability of the morphologies resulting from phase segregation, as well as the ability to modify or control the phase structure obtained. In this investigation, the solvents used were varied and the morphologies obtained were monitored for the G2, G3, and G4 templates previously discussed, as each produced distinct types of intramolecular phase segregation. While toluene was first examined, solvents of increased polarity such as THF and chloroform could potentially pose a problem, since HAuCl$_4$ is soluble in these solvents and selective coordination with the 2VP units may be disrupted. Free metallic salt could complicate microscopic analysis, as the films

would be contaminated with unbound metallic residues decreasing the contrast of the images. Fortunately, this was not an issue, and the films were exclusively populated with metal-loaded arborescent templates even in the presence of more polar solvents, in analogy to PS-*b*-P4VP micellar systems.[46]

Dilution of the toluene solutions of the gold-loaded polymer with an equal volume of THF as a nonselective solvent, to obtain a 1:1 THF/toluene mixture, resulted in no discernible change in morphology for all of the copolymers investigated. The addition of $CHCl_3$ likewise resulted in morphology retention, although less defined toroidal structures were observed for the G2 template. This slight change is attributed to the better solvent quality increasing chain mobility and swelling for the P2VP phase, which was also observed in DPD simulations for the unloaded template molecules (Figure S5a vs Figure S5c).

On loading the same copolymers with 0.5 equiv of $HAuCl_4$/2VP unit in pure $CHCl_3$, a less selective solvent than those previously tested, it resulted in noticeable changes in phase segregation (Figure 4). The G2 template now had a smaller diameter core having the appearance of a dimple, presumably due to enhanced swelling of the P2VP phase. This was accompanied by the formation of better-defined (more complete) and more uniform toroidal species. Since the species were swollen and had a less defined central void, ringlike organization of the metal (as viewed by TEM imaging) was also less obvious than for loading in toluene (compare Figures 3a and 4a). The G3 template did not exhibit any noticeable change in morphology by loading in $CHCl_3$, with raspberry structures similar to those obtained in toluene (Figure 4b). It also appears that some of the intramolecular aggregates merged into longer ones, which was confirmed by the DPD simulations (lower row in Figure 4b). The G4 template appeared to display a morphological transition, however. The continuous cylindrical nanophases observed in toluene (an apolar solvent) became an interpenetrating worm structure in $CHCl_3$. The resulting weaved wormlike appearance, resembling a spherical nanocage, can be seen in Figure 4c. The morphological transition is attributed to increased solvency for P2VP affording a more continuous and uniform phase.

Similar cagelike micelles have been reported for intermolecular micelles of amphiphilic multiblock copolymers,[47] but the structures were much less defined and the morphology was not captured to the degree reported herein. The simulations of Pinna et al. for block copolymer-coated nanoparticles also yielded morphologies similar to Figure 4c, obtained for $HAuCl_4$-loaded G3PS-*g*-(P2VP14-*b*-PS12) in $CHCl_3$, and were referred to as "golf ball" structures.[48] While cell dynamic simulations predicted structures close to our unimolecular system, experimental support for such morphologies is limited. Apart from that, the results of our DPD simulations show that upon loading in $CHCl_3$, such cagelike aggregates are continuous not only within the periphery but also in the inner part of the template molecules (lower row in Figure 4c). This is due to the uniform initial distribution of P2VP domains in chloroform, resulting from the assumption of random grafting of P2VP-*b*-PS chains (Figure S5c).

In view of the results showing the influence on morphology of selective (toluene) and nonselective solvents (THF, $CHCl_3$) for PS, the effects of a solvent selective for P2VP were also investigated. While methanol is a nonsolvent for PS, it is a

known good solvent for P2VP,[7] but the arborescent copolymers should remain soluble in low methanol content solutions. The arborescent copolymers were therefore dissolved in toluene with 2% methanol, loaded with 0.5 equiv of $HAuCl_4$/2VP unit, and then analyzed by TEM (Figure 5) and SFM. The influence of P2VP-selective solvents
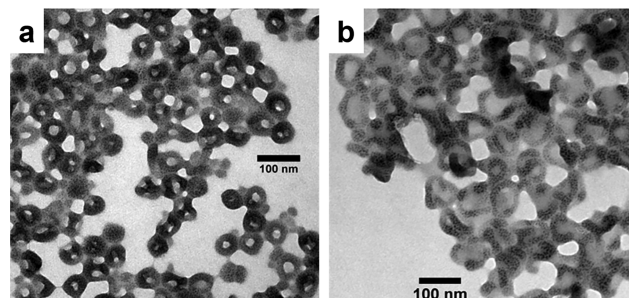

Figure 5. TEM images for arborescent copolymer templates loaded with 0.5 equiv of $HAuCl_4$/2VP unit in toluene with 2% methanol: (a) G2PS-*g*-(P2VP14-*b*-PS12) and (b) G3PS-*g*-(P2VP14-*b*-PS12).

was further investigated by adding more methanol to the gold-loaded polymer solutions until the first indication of colloidal precipitate formation (cloud point at ca. 19% methanol content) for the G1PS-*g*-(P2VP30-*b*-PS20) and G2PS-*g*-(P2VP14-*b*-PS12) copolymers. Methanol-induced morphology changes were observed for the G2 template, which displayed toroidal structures in toluene. Even at only 2% methanol content, a spherical topology was obtained, although central indentations remained for a small number of species. This dimpled sphere morphology was very similar to that for metal coordination in $CHCl_3$ (Figure 4a). Analysis by TEM provided little evidence for ringlike organization of the metal within the templates, proving that phase segregation was altered significantly from a toroidal to a spherical morphology. Microscopy results for these samples can be found in the Supporting Information (Figure S12). No additional morphology changes were observed when loading at increased methanol contents up to the precolloidal dispersion state. Spherical species resulted, again with a small phase differential in the center of the structures.

The G2PS-*g*-(P2VP14-*b*-PS12) and G3PS-*g*-(P2VP14-*b*-PS12) copolymers displayed more interesting morphology changes in the presence of methanol. The G3 template, characterized by a raspberry morphology when loaded with $HAuCl_4$ in toluene or chloroform, underwent a transition to wormlike structures with 2% methanol, as seen in Figure 5a. At higher methanol content, increased domain spacing was observed. The transition to wormlike phase segregation is attributed to enhanced phase separation between PS and P2VP resulting from P2VP swelling by methanol. The interpenetrating PS chains of the substrate, which induced nodular phase separation in toluene, should be excluded from the P2VP phase due to their greater incompatibility with methanol under these conditions. Enhanced phase separation between the PS and the P2VP chains within the G3 template in the presence of methanol is analogous to the situation encountered in the G4 molecules, due to the preferential reaction of coupling sites on the periphery of the substrate, and likewise favors the formation of continuous wormlike domains. In the case of the G4 template, worm-in-sphere morphologies were again observed (Figure 5b) but with increased domain spacing

as compared to toluene alone. Interpenetration between the PS and P2VP phases being already minimized in this system, the addition of methanol had no influence on the morphology.

The final solvent investigated was cyclohexane (CH), which is a θ solvent for PS and a nonsolvent for P2VP, and may therefore also induce interesting phase segregation phenomena. The HAuCl$_4$-loaded copolymers were insoluble in CH alone; thus, a binary solvent system was used with THF. The copolymers were loaded with HAuCl$_4$ (0.5 equiv/2VP) in THF and then diluted with CH to yield either 25 or 75% CH content (Figures S13−S15). In solutions with 25% CH (Figure S13a), G1PS-g-(P2VP30-b-PS20) lost its toroidal topology, as with the addition of methanol. The topology was mainly spherical, but a small number of structures also displayed a central depression. Toroidal phase segregation was nevertheless still observed in the SFM phase scan. TEM analysis yielded similar findings for the metal organization within the polymer scaffold, namely, a circular distribution with some templates having a lower metal concentration at the center. In the binary solvent system containing 75% CH and 25% THF, a spherical topology with uniform metal distribution was exclusively observed by the SFM phase and TEM analysis (Figure S13b). Analogous observations were made for the G3 and G4 templates (Figures S14 and S15, respectively), with the loss of nanodomains and an increased trend toward a spherical morphology at higher CH content.

Along with studies of the impact of the solvent, the influences of the metallic ion type, loading protocol, and intermolecular effects on the final morphologies of the obtained nanoparticles were also determined. These results and discussions can be found in Sections S2.7−S2.9, Supporting Information.

Reduction to Gold Nanoparticles. It is understood that the gold salt (AuCl$_4^-$) contained within the arborescent copolymer molecules, shown in the TEM figures herein, was reduced to elemental gold by the electron beam in TEM analysis. Many other reducing agents and techniques have been proposed for the reduction of gold salts coordinated within polymeric templates, to be more convenient for the production of gold nanoparticles on a large scale. The type and amount of reagent and the reduction protocol used can afford very different outcomes in terms of nanoparticle size and uniformity.[49] Analysis of the average size and/or distribution of the resulting nanoparticles can be performed by microscopic techniques such as TEM or by spectroscopic methods. Since nanoparticles of gold salt (AuCl$_4^-$) and elemental gold (Au^0) have an absorption maximum within the visible wavelength range, UV−vis spectroscopy can serve to monitor changes in the properties of the nanoparticles.

In a previous report,[11] the reduction of HAuCl$_4$ with anhydrous hydrazine was examined in two different regimes and for two different arborescent copolymer templates: near equivalence and in the excess stoichiometry regimes for PS-g-(P2VP16-b-PS12) and G1PS-g-(P2VP30-b-PS20). Aggregation of the nanoparticles was more prevalent in the near-equivalence regime, as larger average sizes and broader size distributions were observed. Since limited quantities of anhydrous hydrazine were available, and handling that compound poses safety risks, its use was limited to these two copolymers. UV−vis characterization for gold salt-loaded and hydrazine-reduced templates can be found in the Supporting Information (Figures S23 and S24). These results were compared with the stronger reducing agent sodium borohy-

dride (NaBH$_4$), as faster reduction can produce smaller nanoparticles that remain localized in their original environment. This effect can be explained by decreased intertemplate metal migration, agglomeration, and Ostwald ripening. Sodium borohydride could therefore represent an interesting solution to preserve the characteristics (morphology) observed for the metallic salt-loaded templates. In each case, NaBH$_4$ was added in excess (10:1 NaBH$_4$/Au) to solutions of the arborescent copolymers loaded with 0.5 equiv of HAuCl$_4$/2VP unit, to ensure fast reduction and minimized agglomeration of the primary nanoparticles formed (the reduction of gold nanoparticles by the different methods is compared in Section 2.10, Supporting Information). The diameter of the gold nanoparticles obtained is summarized in Table 4 and compared with the nanoparticle diameter obtained by anhydrous hydrazine reduction of 0.5 equiv of HAuCl$_4$-loaded templates.

Table 4. Gold Nanoparticle Diameter by Reduction with Anhydrous Hydrazine or NaBH$_4$ at a 10:1 Ratio

	diameter (nm)	
template	NaBH$_4$	N$_2$H$_4$
PS-g-(P2VP16-b-PS12)	4 ± 2	10 ± 3
G0PS-g-(P2VP11-b-PS8)	5 ± 2	
G1PS-g-(P2VP7-b-PS7)	4 ± 1	
G1PS-g-(P2VP30-b-PS20)	4 ± 1	8 ± 2
G2PS-g-(P2VP16-b-PS12)	5 ± 1	
G3PS-g-(P2VP14-b-PS12)	5 ± 1	

As expected, the nanoparticles obtained with NaBH$_4$ were smaller than for hydrazine reduction, but the size dispersity was similar. There was virtually no discernible difference in the UV−vis absorbance spectra for the nanoparticles formed by NaBH$_4$ vs hydrazine reduction of the G1PS-g-(P2VP30-b-PS20) template, with absorption maxima at 521 and 522 nm, respectively. This negligible change, in spite of the very different size of the nanoparticles, may be due to the close proximity of the smaller (4 nm) nanoparticles yielded by NaBH$_4$ (Figure 6b), giving an absorption spectrum similar to the larger (8 nm) nanoparticles obtained with hydrazine.

There is apparently no correlation between the template size (i.e., the overall molecular weight, length of the P2VP segments, or the arborescent polymer generation) and the size of the metallic nanoparticles obtained. This is again consistent with previous findings for hydrazine reduction[11] and in agreement with reports on gold nanoparticles templated with poly(amidoamine) (PAMAM)−poly(ethylene glycol) (PEG) dendrimer-star polymers and reduced with NaBH$_4$.[50] While the nanoparticles derived from NaBH$_4$ are much smaller than for hydrazine reduction (Table 4), they are also better confined to discrete areas defined by the polymeric templates. Intertemplate migration was minimized under these conditions, as indicated by the fact that nearly all of the templates contained measurable nanoparticles. This is in contrast to hydrazine reduction, for which empty (gray-shaded) templates, and others, with varying numbers of nanoparticles were observed (Figure 6). While the reduced particles seemed to retain morphologies similar to the salt-loaded templates, as indicated by the shading pattern, nanoparticle organization within the templates did not appear to follow a unique pattern nor to encompass all of the nanodomains within each template.
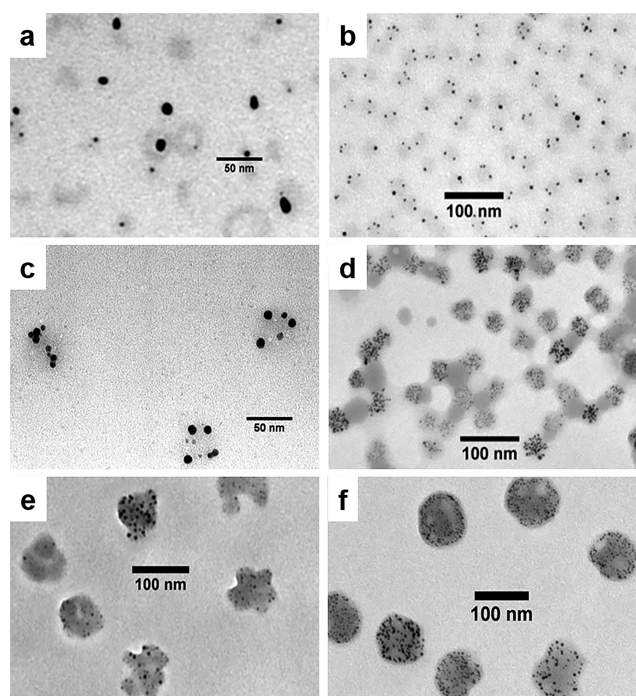
Figure 6. TEM analysis of gold nanoparticles obtained with anhydrous hydrazine or NaBH$_4$ reduction (10:1 ratio) of HAuCl$_4$-loaded PS-*g*-(P2VP16-*b*-PS12) ((a) N$_2$H$_4$, (b) NaBH$_4$), G1PS-*g*-(P2VP30-*b*-PS20) ((c) N$_2$H$_4$, (d) NaBH$_4$), G2PS-*g*-(P2VP14-*b*-PS12) ((e) NaBH$_4$), and G3PS-*g*-(P2VP14-*b*-PS12) ((f) NaBH$_4$).

CONCLUSIONS

We have shown that intramolecular phase segregation with intricate nanodomain formation occurs for arborescent PS-*g*-(P2VP-*b*-PS) core−shell−corona amphipolar copolymers of generations 2 and above upon coordination in selective solvents with various metallic salts and acids, most notably HAuCl$_4$. These unique morphologies were investigated in-depth by SFM and TEM analyses, as well as through mesoscopic computer simulations. For increasing copolymer generations, HAuCl$_4$-induced phase segregation resulted in the formation of disklike structures in G2, then nodular, raspberry-like structures in G3, and finally structures with a worm-in-sphere morphology in G4. In turn, changes in solvent selectivity induced intramolecular morphology changes, which subsequently led to the emergence of new structures after salt loading, and in particular the formation of spherical nanocages in the G4 templates. The physical reason for the emergence of nanomorphologies lies in the high flexibility for the internal structure of arborescent macromolecules. Although the variation in size of the unloaded molecules with the molecular weight displays a hard spherelike proportionality, the mobility of PS and PS−P2VP branches excludes "freezing" of the interior of the arborescent copolymers, allowing them to stay sensitive to external stimuli, in particular solvent quality. The motility of the internal structure, together with the branching motif of the molecular architecture, prevents aggregation of the macromolecules with each other, resulting in intramolecular segregation only. Thus, each macromolecule can be considered as having a "confined" geometry combined with segregation on a nanometer scale. This may be the main reason for the stability of these nonconventional morphologies, in contrast to morphologies formed via aggregation of different macromolecules (e.g., lamellae, ordered cylinders, and

spheres). Thus, arborescent copolymers can be used as effective templates to obtain nanoparticles with complex morphologies, as well as thin metal coatings with a topography tunable at the nanoscale level.

ASSOCIATED CONTENT

Ⓢ Supporting Information

The Supporting Information is available free of charge at https://pubs.acs.org/doi/10.1021/acs.macromol.0c00778.

> Background information, experimental and simulation details, characterization and additional results on metal loading, morphologies, and reduction (PDF)

AUTHOR INFORMATION

Corresponding Authors

Ahmed Mourran − *DWI-Leibniz Institute for Interactive Materials, D-52056 Aachen, Germany;* ⓞ orcid.org/0000-0003-1607-5739; Email: mourran@dwi.rwth-aachen.de

Igor I. Potemkin − *Physics Department, Lomonosov Moscow State University, Moscow 119991, Russian Federation; DWI-Leibniz Institute for Interactive Materials, D-52056 Aachen, Germany; South Ural State University (National Research University), Chelyabinsk 454080, Russian Federation;* ⓞ orcid.org/0000-0002-6687-7732; Email: igor@polly.phys.msu.ru

Mario Gauthier − *Department of Chemistry, Institute for Polymer Research and Waterloo Institute for Nanotechnology, University of Waterloo, Waterloo, Ontario N2L 3G1, Canada;* ⓞ orcid.org/0000-0001-9486-1810; Email: gauthier@uwaterloo.ca

Authors

Jason Dockendorff − *Department of Chemistry, Institute for Polymer Research and Waterloo Institute for Nanotechnology, University of Waterloo, Waterloo, Ontario N2L 3G1, Canada*

Rustam A. Gumerov − *Physics Department, Lomonosov Moscow State University, Moscow 119991, Russian Federation; DWI-Leibniz Institute for Interactive Materials, D-52056 Aachen, Germany;* ⓞ orcid.org/0000-0003-4214-8129

Martin Möller − *DWI-Leibniz Institute for Interactive Materials, D-52056 Aachen, Germany;* ⓞ orcid.org/0000-0002-5955-4185

Complete contact information is available at:
https://pubs.acs.org/10.1021/acs.macromol.0c00778

Author Contributions

The manuscript was written through contributions from all of the authors, who have given their approval for the final version of the manuscript. J.D. and M.G. contributed to the synthesis of the macromolecules, the SFM and TEM measurements, and to the discussion of the results. A.M. and M.M. contributed to the SFM measurements and to the discussion of the results. R.A.G. and I.I.P. contributed to the DPD simulations and also to the discussion of the results.

Notes

The authors declare no competing financial interest.

◼ ABBREVIATIONS

2VP, 2-vinylpyridine; SFM, scanning force microscopy; b, block; CH, cyclohexane; CSC, core–shell–corona; DLS, dynamic light scattering; F, functionalization (mol %); f_w, branching functionality; G, generation; g, graft; M_n, number-average molecular weight; M_w, weight-average molecular weight; P2VP, poly(2-vinylpyridine); P4VP, poly(4-vinylpyridine); PS, polystyrene; DPD, dissipative particle dynamics; r_h, hydrodynamic radius; r_{h1}, hydrodynamic radius from first-order analysis of the correlation function; r_{h2}, hydrodynamic radius from second-order analysis of the correlation function; TEM, transmission electron microscopy; THF, tetrahydrofuran; UV, ultraviolet

◼ REFERENCES

(1) Gauthier, M.; Möller, M. Uniform Highly Branched Polymers by Anionic Grafting: Arborescent Graft Polymers. *Macromolecules* **1991**, *24*, 4548–4553.

(2) Tomalia, D. A. Birth of a New Macromolecular Architecture: Dendrimers as Quantized Building Blocks for Nanoscale Synthetic Polymer Chemistry. *Prog. Polym. Sci.* **2005**, *30*, 294–324.

(3) Cadena, L.-E. S.; Gauthier, M. Phase-Segregated Dendrigraft Copolymer Architectures. *Polymers* **2010**, *2*, 596–622.

(4) Gauthier, M.; Tichagwa, L.; Downey, J. S.; Gao, S. Arborescent Graft Copolymers: Highly Branched Macromolecules With a Core–Shell Morphology. *Macromolecules* **1996**, *29*, 519–527.

(5) Li, J.; Gauthier, M.; Teertstra, S. J.; Xu, H.; Sheiko, S. S. Synthesis of Arborescent Polystyrene-graft-polyisoprene Copolymers Using Acetylated Substrates. *Macromolecules* **2004**, *37*, 795–802.

(6) Puskas, J. E.; Kwon, Y.; Anthony, P.; Bhowmick, A. K. Synthesis and Characterization of Novel Dendritic (Arborescent, Hyperbranched) Polyisobutylene-polystyrene Block Copolymers. *J. Polym. Sci., Part A: Polym. Chem.* **2005**, *43*, 1811–1826.

(7) Dockendorff, J.; Gauthier, M. Synthesis of Arborescent Polystyrene-g-[poly(2-vinylpyridine)-b-polystyrene] Core–Shell–Corona Copolymers. *J. Polym. Sci., Part A: Polym. Chem.* **2014**, *52*, 1075–1085.

(8) Alsehli, M.; Gauthier, M. Arborescent Polypeptides for Sustained Drug Delivery. *MRS Proc.* **2016**, *1819*, No. Imrc2015s4d-o015.

(9) Gauthier, M.; Li, J.; Dockendorff, J. Arborescent Polystyrene-graft-poly(2-vinylpyridine) Copolymers as Unimolecular Micelles. Synthesis from Acetylated Substrates. *Macromolecules* **2003**, *36*, 2642–2648.

(10) Kee, R. A.; Gauthier, M. Arborescent Polystyrene-graft-poly(2-vinylpyridine) Copolymers: Synthesis and Enhanced Polyelectrolyte Effect in Solution. *Macromolecules* **2002**, *35*, 6526–6532.

(11) Dockendorff, J.; Gauthier, M.; Mourran, A.; Möller, M. Arborescent Amphiphilic Copolymers as Templates for The Preparation of Gold Nanoparticles. *Macromolecules* **2008**, *41*, 6621–6623.

(12) Nguon, O.; Gauthier, M.; Karanassios, V. Determination of the Loading and Stability of Pd in an Arborescent Copolymer in Ethanol by Microplasma-Optical Emission Spectrometry. *RSC Adv.* **2014**, *4*, 8978–8984.

(13) Schappacher, M.; Putaux, J. L.; Lefebvre, C.; Deffieux, A. Molecular Containers Based on Amphiphilic PS-b-PMVE Dendrigraft Copolymers: Topology, Organization, and Aqueous Solution Properties. *J. Am. Chem. Soc.* **2005**, *127*, 2990–2998.

(14) Jain, P. K.; Huang, X.; El-Sayed, I. H.; El-Sayed, M. A. Review of Some Interesting Surface Plasmon Resonance-enhanced Properties of Noble Metal Nanoparticles and Their Applications to Biosystems. *Plasmonics* **2007**, *2*, 107–118.

(15) Zeng, S.; Yong, K. T.; Roy, I.; et al. A Review on Functionalized Gold Nanoparticles for Biosensing Applications. *Plasmonics* **2011**, *6*, 491–506.

(16) Garnett, E. C.; Liang, W.; Yang, P. Growth and Electrical Characteristics of Platinum-Nanoparticle-Catalyzed Silicon Nanowires. *Adv. Mater.* **2007**, *19*, 2946–2950.

(17) Qian, X.-M.; Nie, S. M. Single-molecule and Single-nanoparticle SERS: From Fundamental Mechanisms to Biomedical Applications. *Chem. Soc. Rev.* **2008**, *37*, 912–920.

(18) Hoheisel, T. N.; Hur, K.; Wiesner, U. B. Block Copolymer-Nanoparticle Hybrid Self-Assembly. *Prog. Polym. Sci.* **2015**, *40*, 3–32.

(19) Spatz, J. P.; Mössmer, S.; Hartmann, C.; Möller, M.; Herzog, T.; Krieger, S.; Boyen, H.-G.; Ziemann, P.; Kabius, B. Ordered Deposition of Inorganic Clusters from Micellar Block Copolymer Films. *Langmuir* **2000**, *16*, 407–415.

(20) Nachbaur, E.; Leiseder, G. Über Eine Einfache und Gefahrlose Methode zur Darstellung von Wasserfreiem Hydrazin. *Monatsh. Chem.* **1971**, *102*, 1718–1723.

(21) Abramoff, M. D.; Magelhaes, P. J.; Ram, S. J. Image processing with ImageJ. *Biophotonics Int.* **2004**, *11*, 36–42.

(22) Schmitz, C.; Mourran, A.; Keul, H.; Möller, M. Synthesis and Association Behaviour of Linear Block Copolymers with Different Microstructures but the Same Composition. *Macromol. Chem. Phys.* **2008**, *209*, 1859–1871.

(23) Schmitz, C.; Mourran, A.; Keul, H.; Möller, M.; Keerl, M.; Richtering, W. Synthesis and Aggregation Behaviour of Amphiphilic Block Copolymers with Random Middle Block. *Colloid Polym. Sci.* **2009**, *287*, 1183–1193.

(24) Albrecht, K.; Mourran, A.; Zhu, X.; Markkula, T.; Groll, J.; Beginn, U.; de Jeu, W. H.; Moeller, M. Thin Film Morphologies of Block Copolymers Complexed with Wedge-shaped Liquid Crystalline Amphiphilic Molecules. *Macromolecules* **2008**, *41*, 1728–1738.

(25) Hoogerbrugge, P. J.; Koelman, J. M. V. A. Simulating Microscopic Hydrodynamic Phenomena with Dissipative Particle Dynamics. *Europhys. Lett.* **1992**, *19*, 155–160.

(26) Groot, R. D.; Warren, P. B. Dissipative Particle Dynamics: Bridging the Gap Between Atomistic and Mesoscopic Simulation. *J. Chem. Phys.* **1997**, *107*, 4423–4435.

(27) Gumerov, R. A.; Rudov, A. A.; Richtering, W.; Möller, M.; Potemkin, I. I. Amphiphilic Arborescent Copolymers and Microgels: From Unimolecular Micelles in a Selective Solvent to the Stable Monolayers of Variable Density and Nanostructure at a Liquid Interface. *ACS Appl. Mater. Interfaces* **2017**, *9*, 31302–31316.

(28) Maly, M.; Posocco, P.; Pricl, S.; Fermeglia, M. Self-Assembly of Nanoparticle Mixtures in Diblock Copolymers: Multiscale Molecular Modeling. *Ind. Eng. Chem. Res.* **2008**, *47*, 5023–5038.

(29) Posel, Z.; Posocco, P.; Lísal, M.; Fermeglia, M.; Pricl, S. Highly Grafted Polystyrene/Polyvinylpyridine Polymer Gold Nanoparticles in a Good Solvent: Effects of Chain Length and Composition. *Soft Matter* **2016**, *12*, 3600–3611.

(30) Wignall, G. D.; Ballard, D. G. H.; Schelten, J. Measurements of Persistence Length and Temperature Dependence of the Radius of Gyration in Bulk Atactic Polystyrene. *Eur. Polym. J.* **1974**, *10*, 861–865.

(31) Hansen, C. M. *Hansen Solubility Parameters: A User's Handbook*, 2nd ed.; CRC Press: Boca Raton, 2007.

(32) Lindvig, T.; Michelsen, M. L.; Kontogeorgis, G. M. A Flory–Huggins Model Based on the Hansen Solubility Parameters. *Fluid Phase Equilib.* **2002**, *203*, 247–260.

(33) Arras, M. M. L.; He, B.; Jandt, K. D. High Molar Mass Amphiphilic Block Copolymer Enables Alignment and Dispersion of

Unfunctionalized Carbon Nanotubes in Melt-drawn Thin-films. *Polymer* **2017**, *127*, 15−27.

(34) Horsch, M. A.; Zhang, Z.; Iacovella, C. R.; Glotzer, S. C. Hydrodynamics and Microphase Ordering in Block Copolymers: Are Hydrodynamics Required for Ordered Phases with Periodicity in More than One Dimension? *J. Chem. Phys.* **2004**, *121*, 11455−11462.

(35) Santo, K. P.; Vishnyakov, A.; Kumar, R.; Neimark, A. V. Elucidating the Effects of Metal Complexation on Morphological and Rheological Properties of Polymer Solutions by a Dissipative Particle Dynamics Model. *Macromolecules* **2018**, *51*, 4987−5000.

(36) Pal, S. *Pyridine: A Useful Ligand in Transition Metal Complexes*; IntechOpen, 2018.

(37) LAMMPS Molecular Dynamics Simulator. http://lammps.sandia.gov/.

(38) Jha, P. K.; Zwanikken, J. W.; Detcheverry, F. A.; de Pablo, J. J.; de la Cruz, M. O. Study of Volume Phase Transitions in Polymeric Nanogels by Theoretically Informed Coarse-grained Simulations. *Soft Matter* **2011**, *7*, 5965−5975.

(39) Choi, S.; Briber, R. M.; Bauer, B. J.; Topp, A.; Gauthier, M.; Tichagwa, L. Small-angle Neutron Scattering of Solutions of Arborescent Graft Polystyrenes. *Macromolecules* **1999**, *32*, 7879−7886.

(40) Gauthier, M.; Möller, M.; Burchard, W. Structural Rigidity Control in Arborescent Graft Polymers. *Macromol. Symp.* **1994**, *77*, 43−49.

(41) Sheiko, S.; Gauthier, M.; Möller, M. Monomolecular Films of Arborescent Graft Polystyrenes. *Macromolecules* **1997**, *30*, 2343−2349.

(42) Njikang, G. N.; Cao, L.; Gauthier, M. Self-assembly of Arborescent Polystyrene-graft-poly(ethylene oxide) Copolymers at the Air/Water Interface. *Macromol. Chem. Phys.* **2008**, *209*, 907−918.

(43) Mourran, A.; Wu, Y.; Gumerov, R. A.; Rudov, A. A.; Potemkin, I. I.; Pich, A.; Möller, M. When Colloidal Particles Become Polymer Coils. *Langmuir* **2016**, *32*, 723−730.

(44) Potemkin, I. I.; Möller, M. Microphase Separation in Ultrathin Films of Diblock Copolymers with Variable Stickiness of One of the Blocks to the Surface. *Macromolecules* **2005**, *38*, 2999−3006.

(45) Gelissen, A. P. H.; Oppermann, A.; Caumanns, T.; Hebbeker, P.; Turnhoff, S. K.; Tiwari, R.; Eisold, S.; Simon, U.; Lu, Y.; Mayer, J.; Richtering, W.; Walther, A.; Wöll, D. 3D Structures of Responsive Nanocompartmentalized Microgels. *Nano Lett.* **2016**, *16*, 7295−7301.

(46) Antonietti, M.; Wenz, M.; Bronstein, L.; Seregina, M. Synthesis and Characterization of Noble Metal Colloids in Block Copolymer Micelles. *Adv. Mater.* **1995**, *7*, 1000−1005.

(47) Du, B.; Mei, A.; Yong, Y.; Zhang, Q.; Wang, Q.; Xu, J.; Fan, Z. Synthesis and Micelle Behavior of $(PNIPAm-PtBA-PNIPAm)_m$ Amphiphilic Multiblock Copolymer. *Polymer* **2010**, *51*, 3493−3502.

(48) Pinna, M.; Hiltl, S.; Guo, X.; Böker, A.; Zvelindovsky, A. V. Block Copolymer Nanocontainers. *ACS Nano* **2010**, *4*, 2845−2855.

(49) Papp, S.; Kőrösi, L.; Gool, B.; Dederichs, T.; Mela, P.; Möller, M.; Dékány, I. Formation of Gold Nanoparticles in Diblock Copolymer Micelles with Various Reducing Agents: Kinetic and Thermodynamic Studies. *J. Therm. Anal. Calorim.* **2010**, *101*, 865−872.

(50) Hedden, R. C.; Bauer, B. J.; Smith, P. A.; Gröhn, F.; Amis, E. Templating of Inorganic Nanoparticles by PAMAM/PEG Dendrimer−Star Polymers. *Polymer* **2002**, *43*, 5473−5481.

(51) Voevodin, V. V.; Antonov, A. S.; Nikitenko, D. A.; Shvets, P. A.; Sobolev, S. I.; Sidorov, I. Y. u.; Stefanov, K. S.; Voevodin, V. V.; Zhumatiy, S. A. Supercomputer Lomonosov-2: Large Scale, Deep Monitoring and Fine Analytics for the User Community. *Supercomput. Front. Innovations* **2019**, *6*, 4−11.